High-Precision Tracking Control of a Segmented Stator Permanent Magnet Linear Synchronous Motor

Gerd Fuchs, *Graduate Student Member, IEEE*, Andreas Deutschmann-Olek, *Member, IEEE*, Andreas Kugi, *Senior Member, IEEE*, and Wolfgang Kemmetmüller, *Member, IEEE*

***Abstract*—Permanent magnet linear synchronous motors (PMLSMs) are widely used in modern industrial applications, especially in industrial transportation, processing, and manufacturing processes, where high-precision position tracking is vital. By employing a segmented stator design with curvilinear segments, one can achieve complex PMLSM geometries. However, this innovative design introduces challenges in control strategies due to mounting and manufacturing tolerances during final assembly at the customer's site. This article introduces an iterative learning-based high-precision position tracking control strategy to overcome these challenges. Our approach features a subordinate optimal force controller based on a magnetic equivalent circuit model, which adeptly handles nonlinear effects, such as magnetic saturation and cogging force. Calculating optimal currents ensures precise tractive force tracking and minimize ohmic losses, thereby increasing motor efficiency. We implement a two-degree-of-freedom position control strategy that surpasses the performance of traditional field-oriented control when combined with the optimal force controller. Despite this, larger position-tracking errors can occur during segment transitions. Accurately modeling these transitions is impractical due to the inherent errors from mounting and manufacturing tolerances. Therefore, we incorporate an iterative learning control strategy trained on the final setup to achieve exceptional position tracking across the entire curvilinear PMLSM. Experimental results from our test bench reveal remarkable accuracies within 20 μm, demonstrating the method's robustness against manufacturing tolerances.**

***Index Terms*—Iterative learning control (ILC), motion control, permanent magnet linear synchronous motor (PMLSM), position control, segmented stator.**

I. Introduction

In MODERN high-performance industrial applications, permanent magnet linear synchronous motors (PMLSM) are indispensable due to their high performance and flexibility. In particular, linear motors whose stators are composed of a sequence of different segment types (segmented stator linear motors) offer the unique advantage of realizing complex linear motor setups [1]. Moreover, PMLSMs provide the exceptional ability for multiple moving units (shuttles) to operate simultaneously at different speeds at the motor setup [2], [3]. These advantages are particularly significant in industrial transportation, processing, and manufacturing [4], [5], [6].

A cascaded control structure is typically employed to adopt motion control in PMLSMs utilizing a subordinate current or force control loop and a superimposed speed and/or position control loop. For the subordinate current or force control loop, control strategies based on the dq0-transformation, assuming fundamental sinusoidal behavior of the motor quantities, are frequently employed [7], [8]. This approach transforms sinusoidal three-phase quantities to constant quantities, thus yielding simple structures for the current or force control in field-oriented control (FOC) strategies [9], [10], [11]. However, the main limitation of these methods is that nonlinear effects, such as magnetic saturation or force ripple due to reluctance forces or end-effects are not systematically covered, which reduces the achievable control performance. Direct thrust force control is another common control technique for PMLSMs where the switching of the power semiconductors is obtained by switching tables [12], [13], [14]. The advantage of this method is that the control inputs can be obtained computationally fast. However, fast sampling times are needed to achieve a low tracking error and small force ripple. When nonlinear effects such as magnetic saturation are considered, optimization techniques are employed to calculate respective current patterns [15], [16], [17]. These methods consider the required current to generate a tractive force and also pursue secondary objectives, such as minimizing the ohmic losses and thus increasing the motor's energy efficiency.

In order to address the shortcomings of the dq0-transformation-based control strategies, additional measures are frequently taken in the superimposed speed and/or position control loop [18]. In [19] and [20], the force ripple is modeled as the sum of harmonic functions, and the respective parameters are identified. A state-periodic adaptive control method was proposed in [21] using the last iteration information to update the current adaptation law. This method employs a Lyapunov-based approach involving complex nonlinear functions that require intricate tuning for the feedback and adaptation law. It only considers friction and cogging forces in the adaptation, which makes this approach less favorable. Disturbance observers (DOBs) are proposed in [22] and [23] where a disturbance model is

Received 16 December 2024; revised 11 March 2025 and 7 May 2025; accepted 9 June 2025. Date of publication 12 June 2025; date of current version 5 August 2025. This work was supported by the B&R Industrial Automation GmbH. Recommended for publication by Associate Editor J.-B. He. *(Corresponding author: Gerd Fuchs.)*

Gerd Fuchs, Andreas Deutschmann-Olek, and Wolfgang Kemmetmüller are with the Automation and Control Institute, TU Wien, 1040 Vienna, Austria (e-mail: fuchs@acin.tuwien.ac.at; deutschmann@acin.tuwien.ac.at; kemmetmueller@acin.tuwien.ac.at).

Andreas Kugi is with the Automation and Control Institute, TU Wien, 1040 Vienna, Austria, and also with the Austrian Institute of Technology (AIT), Gieffinggasse 4, 1220, Vienna, Austria (e-mail: kugi@acin.tuwien.ac.at).

Color versions of one or more figures in this article are available at https://doi.org/10.1109/TPEL.2025.3579258.

Digital Object Identifier 10.1109/TPEL.2025.3579258

utilized to estimate the disturbance. These methods perform well when the disturbance along the entire motor can be modeled by a single set of parameters, which is typically not the case, especially for segmented stator linear motors. Recently, iterative learning control (ILC) [24], [25], [26] gained attention for suppressing disturbances in PMLSMs during repetitive tasks. Also, combinations of DOB and ILC are proposed in [27], [28], and [29]. Even though good results can be achieved with an ILC that learns a correction over the entire motor length (in contrast to [24], where parameters of harmonic functions are identified via an ILC approach), none of the methods considers shuttles with rollers rather than air or ball bearings. Rollers pose additional challenges due to the disturbances they introduce, such as vibrations and wear. Moreover, only low-performance trajectories with comparably low accelerations and decelerations, velocities, and movement lengths are considered. Also, only a few variations in the trajectories are examined, mainly focused on one fixed trajectory with one constant speed level.

Only limited attention was given the effects of a segmented stator in linear motor designs. In [30] and [31] models for the influence stemming from a stator segmentation are obtained, and a feedforward control is introduced in [32] and [33] to compensate for the cogging force arising from a segmented stator. However, a special setup with coupled shuttles is necessary to apply the method described in [33]. Here, the cogging force is estimated from the currents of the active shuttle, making the method cumbersome to implement. In [32], the cogging force is obtained via finite element analysis, which has the significant limitation that it cannot easily account for a model-plant mismatch. None of the mentioned methods accounts for the manufacturing or mounting tolerances of the segments, thus leading to lower control accuracy in real-world industrial applications.

This article presents a high-precision position tracking method for segmented stator PMLSM setups with curvilinear tracks. The proposed method is not restricted to (higher order) harmonic disturbances; it exhibits low complexity and low computational costs, and no additional telemetry is necessary, facilitating the method's applicability to industrial PMLSM setups, particularly at the final motor setup after assembly. The main contributions of the present work can be summarized as follows:

1) The optimal force control strategy previously developed by the authors for straight segments (SSs) [16] is extended to curved segments based on the highly accurate magnetic equivalent circuit (MEC) model for the curved segments presented in the authors' publication [34]. While the fundamental methodology for calculating the optimal current patterns follow the approach from [16], the contribution of this work lies in the application of this methodology to the curved segments, including the calculation of the optimal current patterns, flux linkages, and inductances for the stator coils, as well as their systematic presentation and analysis, taking into account the significantly different magnetic behavior of the curved segments compared to SSs. Besides improved accuracy in force tracking, an improvement in the energy efficiency of the PMLSM is obtained compared to the state-of-the-art.
2) The second contribution is improving the position-tracking accuracy for each stator segment. Good position tracking results are already obtained by utilizing the optimal current patterns in combination with a two-degree-of-freedom position controller. However, errors arise from manufacturing and mounting tolerances of the actual PMLSM setup. To account for these errors and further increase the position tracking performance, the position controller is augmented by an ILC strategy, enabling high-precision motion for each segment type.
3) The third contribution relates to the high-precision position tracking at the segment transitions. Since the stator segments are assembled manually at the final motor setup, this process is prone to introduce deviations between each motor setup. Thus, it is difficult to derive a highly accurate mathematical model for these segment transitions, yielding larger position tracking errors compared to the errors within the stator segments. Therefore, an ILC strategy is applied again, allowing compensation for these errors and achieving high-precision position tracking at the segment transitions.

The rest of this article is organized as follows: The MEC model is briefly summarized in Section II. Section III presents the control strategy, where Section III-A presents the calculation of the optimal currents for the curved segments, and Sections III-B, III-C, and III-D explain the current controller, position controller, and ILC. The validation of the presented method on a test bench is shown in Section IV. The article closes with the conclusions in Section V.

II. Model of the PMLSM

In this work, the PMLSM models previously developed by the authors are used [34], [35]. Therefore, only the main findings are briefly revisited in this section. The considered PMLSM consists of n_c coils mounted on coil teeth separated by auxiliary teeth. A pulsewidth modulated (PWM) MOSFET half-bridge can control each coil independently. On one side, the coils are connected to their respective half-bridge; on the other, they are connected to a voltage source (balancer) that provides half of the supply voltage $v_\mathrm{dc}/2$. The moving part of the motor (shuttle) comprises five NdFeB-permanent magnets mounted in alternating magnetization orientation on a back iron. Since the shuttle is held on the stator solely by magnetic force, no electrical connection is necessary between the stator and the shuttle. Hence, purely passive shuttles are employed. The x-coordinate denotes the tangential position along the stator edge at the air gap, and the shuttle position along this coordinate is denoted by x_s. The shuttle is guided along the guiding rails with four rollers; see Fig. 1. The actual air gap length is denoted by y_s, the stator period by ν_s, and the shuttle position normalized by the stator period by $x_\mathrm{s}/\nu_\mathrm{s}$. A sketch of the considered PMLSM, which is based on the ACOPOStrak system from B&R Industrial Automation GmbH [36], is depicted in Fig. 2.

The coils of the linear motor are arranged in segments. Three different segment types are considered in this work: an SS, a curve segment (CS), and a circular arc segment (CAS). All three segment types are structurally built equally, see Fig. 2.

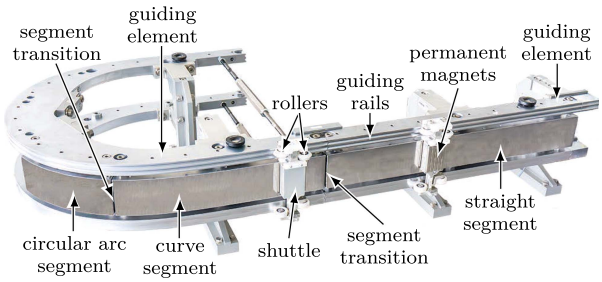

Fig. 1. Picture of the PMLSM setup.

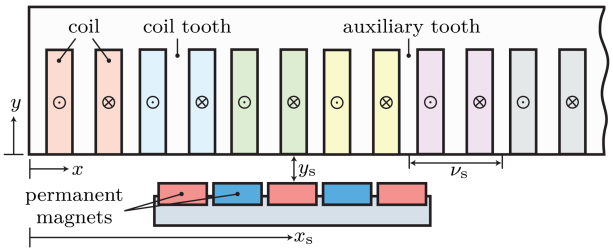

Fig. 2. Sketch of the considered PMLSM [35], [37].

The difference is in the curvature. The SS has no curvature, and the CAS has a constant curvature over the entire segment length. The CS constitutes a transition from an SS to a CAS, i.e., on one side, the CS is straight, whereas on the other, the curvature is equal to that of the CAS. With the combination of these three segment types, it is possible to realize complex linear motor setups. The segments are mounted inside guiding elements, and an air gap exists between each segment instead of an auxiliary tooth (segment transition, see Fig. 1). The width of this segment transition can vary within specific tolerances due to manufacturing and the manual assembly process of the final motor setup. The SS is mounted inside one guiding element, while the CS and CAS are mounted inside another. This leads to a mechanical interface between the two guiding elements, which are, in practice, not perfectly aligned.

A highly accurate MEC model of the SS was derived and extended to curved segments by the authors in [35] and [34], respectively. Therein, a differential MEC model for the stator of the PMLSM was derived, and the resulting differential equations were approximately solved using the numerically efficient pseudospectral method [38], [39]. A lumped-parameter model of permeances and magnetomotive force (mmf) sources models the shuttle. Position-dependent air gap performances attain the coupling between the stator and the shuttle. The models were calibrated with measurements, and high model accuracy was achieved for all considered segment types (SS, CS, and CAS) of the linear motor for the entire motor operation range. These models systematically consider nonlinear effects, such as magnetic saturation and cogging force and can be solved numerically efficiently, particularly compared to finite element models. Therefore, these models are an appropriate basis for the following model-based controller design.

The overall model of the PMLSM is given by the differential algebraic equation [34]

$$\frac{\mathrm{d}\boldsymbol{\psi}_\mathrm{c}}{\mathrm{d}t} = -\mathbf{R}_\mathrm{c}\mathbf{i}_\mathrm{c} + \mathbf{v}_\mathrm{c} \tag{1a}$$

$$\mathbf{0} = \mathbf{K}(\mathbf{z})\mathbf{z} - \mathbf{B}(\mathbf{i}_\mathrm{c}) \tag{1b}$$

with the electric coil voltages $\mathbf{v}_\mathrm{c}$, the coil currents $\mathbf{i}_\mathrm{c}$, the diagonal matrix of the coil resistances $\mathbf{R}_\mathrm{c}$, the magnetic flux linkages $\boldsymbol{\psi}_\mathrm{c}$, and $\mathbf{z}^\mathrm{T} = [\hat{\boldsymbol{\phi}}^\mathrm{T}, \hat{\boldsymbol{\varphi}}^\mathrm{T}, \mathbf{u}_\mathrm{tg}^\mathrm{T}, \boldsymbol{\psi}_\mathrm{c}^\mathrm{T}]$, where $\hat{\boldsymbol{\phi}}$ holds the approximated magnetic fluxes, $\hat{\boldsymbol{\varphi}}$ the approximated magnetic potentials, and $\mathbf{u}_\mathrm{tg}$ the mmf of the tree permeances of the MEC. $\mathbf{K}$ and $\mathbf{B}$ in (1) contain the equations for the stator model, shuttle model, the network equations, and the relation between the fluxes and flux linkages; see [34] and [35] for further details. The tractive force τ_x and the normal force τ_y of the shuttle are obtained by using the coenergy principle [40]

$$\tau_x = \frac{1}{2}\mathbf{u}_\mathrm{tg}^\mathrm{T}\frac{\partial \boldsymbol{\mathcal{G}}_\mathrm{t}}{\partial x_\mathrm{s}}\mathbf{u}_\mathrm{tg} + \frac{1}{2}\mathbf{u}_\mathrm{c}^\mathrm{T}\frac{\partial \boldsymbol{\mathcal{G}}_\mathrm{c}}{\partial x_\mathrm{s}}\mathbf{u}_\mathrm{c} \tag{2a}$$

$$\tau_y = \frac{1}{2}\mathbf{u}_\mathrm{tg}^\mathrm{T}\frac{\partial \boldsymbol{\mathcal{G}}_\mathrm{t}}{\partial y_\mathrm{s}}\mathbf{u}_\mathrm{tg} + \frac{1}{2}\mathbf{u}_\mathrm{c}^\mathrm{T}\frac{\partial \boldsymbol{\mathcal{G}}_\mathrm{c}}{\partial y_\mathrm{s}}\mathbf{u}_\mathrm{c} \tag{2b}$$

with the vector $\mathbf{u}_\mathrm{c}$ containing the mmfs of the cotree, and the diagonal matrices $\boldsymbol{\mathcal{G}}_\mathrm{t}$ and $\boldsymbol{\mathcal{G}}_\mathrm{c}$ containing the (position-dependent) tree and cotree permeances, respectively. For more details, the reader is referred to [34] and [35].

The mechanical behavior of the shuttle is described by

$$(m_\mathrm{s} + m_\mathrm{L})\,\ddot{x}_\mathrm{s} = \tau_x - k_\mathrm{c}\tanh\left(\frac{\dot{x}_\mathrm{s}}{\bar{v}_\mathrm{c}}\right) - k_\mathrm{d}\dot{x}_\mathrm{s} \tag{3}$$

with the shuttle mass m_s, the mass of the load m_L, the viscous damping coefficient k_d, and the model of the Coloumb friction $k_\mathrm{c}\tanh(\dot{x}_\mathrm{s}/\bar{v}_\mathrm{c})$, with the parameters k_c and $\bar{v}_\mathrm{c}$.

III. Control Strategy

In this section, a model-based control strategy based on the model introduced in Section II is developed. First, the optimal force control strategy presented in the authors' previous publication [16] is extended to the curved segments. Second, a two-degree-of-freedom position controller is introduced, similar to the one used in the authors' works [16], [37]. Finally, an ILC is designed to account for errors arising from a model-plant mismatch, thus enabling high-precision position tracking throughout the entire curvilinear track of the linear motor setup, i.e., inside the segments and at the segment transitions.

A. Optimal Currents for the Curved Segments

In order to generate a tractive force τ_x and, if necessary (e.g., at diverters), a specific normal force τ_y on the shuttle, an optimal force controller is employed. Since no force sensor is present, the indirect force control strategy for SSs presented in the authors' previous publication [16] is extended to curved segments in this work. This contribution discusses the current patterns for the curved segment of the PMLSM since one cannot simply infer them from the SS presented in [16].

Each coil of the PMLSM can be controlled separately. This yields more degrees of freedom than necessary for generating a desired tractive force τ_x^{d} at the shuttle. Hence, secondary control goals can be considered. An optimization problem is formulated with the following goals:

1) The primary goal is that the resulting tractive τ_x and normal forces τ_y track the desired values τ_x^{d} and τ_y^{d} as accurately as possible.
2) The ohmic losses, and therefore also the thermal losses, i.e., $\mathbf{i}_{\mathrm{c}}^{\mathrm{T}}\mathbf{i}_{\mathrm{c}}$, should be minimized to achieve an energy-efficient motor operation.
3) To minimize the load on the balancer, the sum current $i_\Sigma = \sum_{\ell=1}^{n_{\mathrm{c}}} i_{\mathrm{c},\ell}$ should be minimized.

These considerations lead to the optimization problem

$$\min_{\mathbf{z},\mathbf{i}_{\mathrm{c}}} \quad J(\mathbf{z},\mathbf{i}_{\mathrm{c}}) = k_i \mathbf{i}_{\mathrm{c}}^{\mathrm{T}}\mathbf{i}_{\mathrm{c}} + k_\Sigma i_\Sigma^2 + k_x \left(\tau_x^{\mathrm{d}} - \tau_x\left(\mathbf{z},\mathbf{i}_{\mathrm{c}}\right)\right)^2 + k_y \left(\tau_y^{\mathrm{d}} - \tau_y\left(\mathbf{z},\mathbf{i}_{c}\right)\right)^2 \tag{4a}$$

$$\text{s.t.} \quad \mathbf{g}(\mathbf{z},\mathbf{i}_{\mathrm{c}}) = \mathbf{K}(\mathbf{z})\mathbf{z} - \mathbf{B}(\mathbf{i}_{\mathrm{c}}) = \mathbf{0} \tag{4b}$$

with the positive weighting factors k_i, k_Σ, k_x, and k_y. Note that the objective of tracking the desired forces, i.e., τ_x^{d} and τ_y^{d}, could also be considered as equality constraints in (4). However, the presented approach has the advantage that it is numerically more efficient and that the weighting factors can weigh the different goals. However, the proposed approach already delivers accurate tracking behavior, and demanding exact tracking of the forces in the optimization problem does not lead to a better tracking performance in the considered operating scenarios due to inevitable model-plant mismatch. Even though the optimization task can be solved numerically very efficiently, it is not real-time capable within one sampling period of the current controller $T_{\mathrm{s},i} = 25\ \mu\mathrm{s}$. Therefore, (4) is solved offline by employing the MATLAB function `fmincon` for the desired forces $\tau_{x,\zeta}^{\mathrm{d}} = -\tau_{x,\max} + 2\zeta\tau_{x,\max}/N_\tau$, $\zeta = 0,\ldots,N_\tau$, with the maximum force $\tau_{x,\max}$ and the number of force values N_τ, on a shuttle position grid $x_{\mathrm{s},\zeta}^i = \bar{x}_{\mathrm{s}}^i + \zeta\Delta_x^i$, $\zeta = 0,\ldots,N_{\mathrm{x}}^i$, with the start position of the grid $\bar{x}_{\mathrm{s}}^i$, the grid width Δ_x^i, and the total number of grid points N_{x}^i, to obtain the optimal currents $\mathbf{i}_{\mathrm{c}}^*$ and optimal flux linkages $\boldsymbol{\psi}_{\mathrm{c}}^*$. Similar to the SS (see [16]), it is sufficient to solve the optimization problem for one stator period ν_{s} for the CAS since the currents for the other coils can be obtained by a respective shift by ν_{s} due to the symmetry of the segment. In contrast, the currents have to be calculated for each coil of the CS due to the changing curvature, see [34]. The efficient model evaluation presented in [34] provides a framework for numerically efficient calculation of the optimal currents and flux linkages for the CS. The optimization results are stored in lookup tables (LUTs).

For the following results, the tracking of the normal force is omitted in the optimization, i.e., $k_y = 0$, since it is not essential for this work.[1] In Fig. 3(a), the results of the optimization are depicted for $\tau_x^{\mathrm{d}} = 20$ N for the SS, for the CAS, and two coils of the CS (coil 20 and coil 25). Moreover, the current pattern for classical FOC is shown for $\tau_x^{\mathrm{d}} = 20$ N as a comparison. Note that the midpoints of the current patterns are shifted to zero for the sake of comparison in this plot. It can be seen that the currents differ for each segment, and in the CS, the coil currents for each coil are slightly different. Moreover, it is visible that six coils are utilized for the optimal current patterns. Note that only four coils would be sufficient to generate the tractive force on the shuttle, but following [16], it is meaningful to use six coils if the sum current i_Σ should be minimized. Hence, only six currents must be considered when calculating the optimal currents at each grid point. The comparison with the FOC current pattern reveals that the amplitude of the FOC current is constant for constant desired forces, in contrast to the optimal currents. It is worth noting that the fundamental frequency of the FOC current is in the range of 100 Hz for a shuttle velocity of $\dot{x}_{\mathrm{s}} = 2$ m/s. This also shows that the average ohmic losses, i.e., $1/\bar{N}_{\mathrm{x}}^i \sum_{j=1}^{\bar{N}_{\mathrm{x}}^i} R_{\mathrm{c}} i_{\mathrm{c}}^2(x_{\mathrm{s},j})$, with the number $\bar{N}_{\mathrm{x}}^i$ of samples along the shuttle position, are larger for the FOC currents. For $\tau_x^{\mathrm{d}} = 20$ N, this is 1.97 W and 1.24 W for FOC and the optimal currents of the CAS, respectively. A more detailed investigation of the ohmic losses is presented in Section IV-B. Fig. 3(b) shows the optimization results for the CAS for different values of τ_x^{d}. In this plot, it is noteworthy that the current for $\tau_x^{\mathrm{d}} = 0$ N resembles the current necessary to compensate for the force ripple. Moreover, the resulting optimal currents deviate significantly from a fundamental sinusoidal form to account for the nonlinear behavior of the motor.

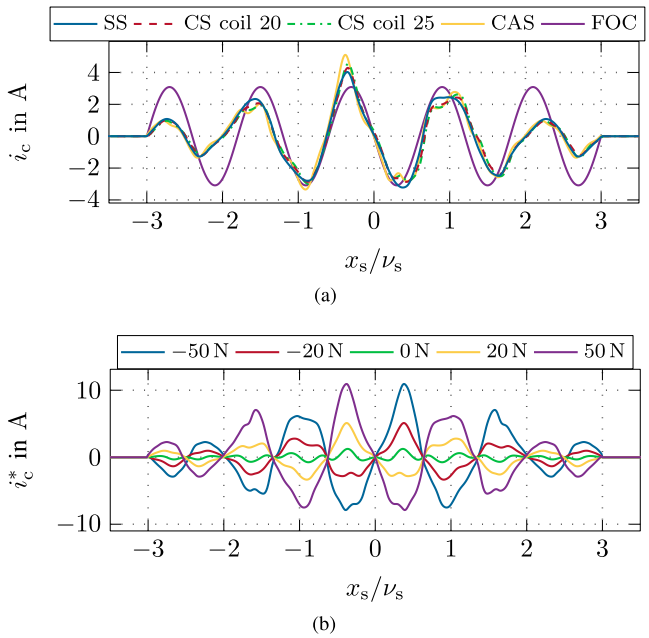

Fig. 3. Optimal currents $\mathbf{i}_{\mathrm{c}}^*$ with $k_i = 1, k_\Sigma = 50, k_x = 100, k_y = 0$ for (a) $\tau_x^{\mathrm{d}} = 20$ N comparing the SS, two coils of the CS and the CAS, together with a current for FOC and (b) for different desired tractive forces τ_x^{d} at the CAS.

B. Current Controller

As described in the authors' previous work [16], the optimal currents $\mathbf{i}_{\mathrm{c}}^*$ calculated in Section III-A are used in a current

[1] The adjustment of the normal force is mainly relevant for track switches, where the shuttle is moved from one track to another.

controller, which is designed based on the model (1) and comprises a feedforward $\mathbf{v}_\mathrm{c}^\mathrm{ff}$ and a feedback $\mathbf{v}_\mathrm{c}^\mathrm{fb}$ part yielding the control law $\mathbf{v}_\mathrm{c} = \mathbf{v}_\mathrm{c}^\mathrm{ff} + \mathbf{v}_\mathrm{c}^\mathrm{fb}$ with

$$\mathbf{v}_\mathrm{c}^\mathrm{ff} = \frac{\mathrm{d}\boldsymbol{\psi}_\mathrm{c}^*}{\mathrm{d}t} + \mathbf{R}_\mathrm{c}\mathbf{i}_\mathrm{c}^* \tag{5a}$$

$$\mathbf{v}_\mathrm{c}^\mathrm{fb} = -\mathbf{R}_\mathrm{c}\mathbf{e}_i + \mathbf{L}(\mathbf{i}_\mathrm{c}^*, x_\mathrm{s})\left(c_\mathrm{p}^i\mathbf{e}_i + c_\mathrm{I}^i\int_0^t \mathbf{e}_i\,\mathrm{d}\tau\right) \tag{5b}$$

with the current error $\mathbf{e}_i = \mathbf{i}_\mathrm{c}^* - \mathbf{i}_\mathrm{c}$ and the inductance matrix $\mathbf{L}$, see [16] for further details. Due to the presence of an auxiliary tooth between the coils, the coupling inductances can be neglected. Thus, $\mathbf{L}$ is diagonal, leading to n_c decoupled current controllers. The choice $c_\mathrm{p}^i, c_\mathrm{I}^i > 0$ renders the closed-loop tracking error dynamics exponentially stable [41]. Note that $\mathrm{d}\boldsymbol{\psi}_\mathrm{c}^*/\,\mathrm{d}t \approx (\partial\boldsymbol{\psi}_\mathrm{c}^*/\partial x_\mathrm{s})\dot{x}_\mathrm{s}$ is used in (5a) (c.f., [16]), where $\partial\boldsymbol{\psi}_\mathrm{c}^*/\partial x_\mathrm{s}$ is calculated numerically from the solution of (4) and also stored in an LUT, such as the optimal currents $\mathbf{i}_\mathrm{c}^*$.

Since only six coils are necessary to generate the current patterns for one shuttle, only six current controllers around each shuttle must be active at a time. After the shuttle traveled one stator period ν_s, the current controller of the coil that leaves the shuttle region gets reset and is used for the coil that newly enters the shuttle region. This significantly reduces the number of active controllers, especially for large motor setups where the shuttles are not densely packed on the motor. Note that for the inactive coils; the half bridges are switched off, reducing the switching losses.

C. Position Controller

A position controller similar to the one derived by the authors in [16] and [37] controls the shuttle motion along the stator. A flatness-based control strategy with a feedforward part τ_x^ff and a feedback part τ_x^fb based on (3) is employed, yielding the control law $\tau_x^\mathrm{c} = \tau_x^\mathrm{ff} + \tau_x^\mathrm{fb}$ with

$$\tau_x^\mathrm{ff} = (m_\mathrm{s} + m_\mathrm{L})\,\ddot{x}_\mathrm{s}^\mathrm{d} + k_\mathrm{c}\tanh\left(\frac{\dot{x}_\mathrm{s}^\mathrm{d}}{\bar{v}_\mathrm{c}}\right) + k_\mathrm{d}\dot{x}_\mathrm{s}^\mathrm{d} \tag{6a}$$

$$\tau_x^\mathrm{fb} = (m_\mathrm{s} + m_\mathrm{L})\left(c_\mathrm{d}^x\left(\dot{x}_\mathrm{s}^\mathrm{d} - \dot{x}_\mathrm{s}\right) + c_\mathrm{p}^x\left(x_\mathrm{s}^\mathrm{d} - x_\mathrm{s}\right) + c_\mathrm{I}^x\int_0^t\left(x_\mathrm{s}^\mathrm{d} - x_\mathrm{s}\right)\mathrm{d}\tau\right) \tag{6b}$$

with the twice continuously differentiable desired trajectory $x_\mathrm{s}^\mathrm{d}(t)$. A proper choice of the control parameters $c_\mathrm{d}^x, c_\mathrm{p}^x, c_\mathrm{I}^x > 0$ renders the position tracking error $e_x = x_\mathrm{s}^\mathrm{d} - x_\mathrm{s}$ asymptotically stable [41].

The position controller (6), combined with the optimal current patterns and the subordinate current controller (5), delivers good results inside the segments. However, more significant control errors are present at the segment transitions. This is due to a larger model-plant mismatch in the force-to-current mapping since the segment transitions (air gap instead of an auxiliary tooth) are not explicitly considered in the MEC model and, hence, not in calculating the optimal currents. In principle, it would be possible to incorporate the segment transitions in the MEC model and the subsequent calculations of the optimal currents. However, this would significantly increase the model complexity. Furthermore, since the air gap at the segment transitions depends on the actual mounting of the segments, a calibration after assembling the final motor setup would be necessary, which renders this method infeasible for practical usage. To address these issues, an ILC approach that relies only on internal position measurement is proposed in this work to improve position-tracking performance.

D. Iterative Learning Control

A stochastically optimal ILC approach [42] is employed in this work. This approach allows for systematic calculation of the learning filter based on the knowledge of the plant model (3), sensor noise, and the spectral properties of the expected error. Note that, in principle, other ILC approaches can also be used since the main purpose of the ILC is to drive the error (close) to the measurement noise level. However, the stochastically optimal ILC approach is employed due to the above-mentioned benefits.

Due to the feedforward part of the position controller (6a), the friction can be neglected, and the plant model (input force τ_x, output position x_s) reads as $G(s) = 1/(m_\mathrm{s}s^2)$, where s denotes the Laplace variable from the bilateral Laplace transform. The feedback part of the position controller (6b) is given by

$$R(s) = m_\mathrm{s}\frac{c_\mathrm{d}^x s^2 + c_\mathrm{p}^x s + c_\mathrm{I}^x}{s}. \tag{7}$$

Here, only the shuttle mass m_s is considered, i.e., the ILC design is based on the nominal operation without an additional load mass. A discussion on how to easily account for the load mass will be presented later. Employing the methodology detailed in [42], we design the learning filter $L(s)$ of the ILC in the form

$$L(s) = \frac{S^{\nu\nu}(s)H(-s)}{H(s)S^{\nu\nu}(s)H(-s) + S^{ww}(s)} \tag{8}$$

with the transfer function $H(s)$ from the ILC output τ_x^ilc to the ILC input e_x given by $H(s) = G(s)/(1 + R(s)G(s))$. The stochastic properties of the position sensor are modeled as white noise $S^{ww}(s) = T_{\mathrm{s},x}\sigma_{x_s}^2/2$, with the measured noise power $\sigma_{x_s}^2$ and the sampling time $T_{\mathrm{s},x}$ of the position sensor. Since relevant errors occur mainly below the frequency ω_c, the input error power spectral density is modeled by

$$S^{\nu\nu}(s) = \frac{V}{\left(1 + \frac{s}{\omega_\mathrm{c}}\right)^4\left(1 - \frac{s}{\omega_\mathrm{c}}\right)^4} \tag{9}$$

with the cutoff frequency ω_c and the gain V. These parameters are used to influence the learning behavior of the ILC. The gain V influences the entire learning bandwidth and the learning speed of the ILC (by increasing V, the bandwidth and learning speed are increased), while the cutoff frequency ω_c is chosen such that high-frequency errors are ignored in the learning. Higher frequency errors of relevant size mainly occur at high shuttle velocities. The force learned by the ILC τ_x^ilc would also contain these high frequencies and thus would lead to high frequencies in the desired currents. The current controller

would then require very large coil voltages, which are limited by the supply voltage v_{dc}. Therefore, it is meaningful to neglect high-frequency components of the error in the ILC, which is guaranteed by an appropriate choice of the cutoff frequency, i.e., $\omega_{\mathrm{c}} = 2\pi 150$ rad/s in this application. The low-pass filter of order 4 in (9) provides sufficient attenuation of frequencies above ω_{c} to prevent reaching the coil voltage limitation through the ILC, and a higher order low-pass filter would not offer additional benefits.

The inverse Fourier transform is applied to (8) to obtain the learning filter in the time domain

$$L_t(t) = \mathcal{F}^{-1}\left\{L(\mathrm{I}\omega)\right\} \tag{10}$$

where I denotes the imaginary unit. The impulse response of the learning filter is depicted in Fig. 4. Note that the resulting filter is noncausal. The learning filter (10) is discretized with the sampling time $T_{\mathrm{s},x}$ for $-\kappa, \ldots, \kappa$ sampling points $\mathbf{\Gamma} = [L_t(-\kappa T_{\mathrm{s},x}), \ldots, L_t(\kappa T_{\mathrm{s},x})]$ to implement the learning law

$$\tau_{x,k}^{\mathrm{ilc},j+1} = \tau_{x,k}^{\mathrm{ilc},j} + \alpha_k T_{\mathrm{s},x} \mathbf{\Gamma} \left[e_{x,k+\kappa+\delta}^{j}, \ldots, e_{x,k-\kappa+\delta}^{j}\right]^{\mathrm{T}} \tag{11}$$

for the sampling point $t = kT_{\mathrm{s},x}$, with the convolution of the learning filter with the position error $e_x^j = x_{\mathrm{s}}^{\mathrm{d}} - x_{\mathrm{s}}^{j}$ in a sample-based real-time system. Therein, j denotes the iteration index of the ILC, δ a time delay to approximately account for the deadtime of the measurement, and $\alpha_k \in (0, 1]$ a damping factor to increase the robustness of the learning, e.g., in the case of model-plant mismatch. Moreover, the ILC is initialized by $\tau_{x,k}^{\mathrm{ilc},0} = 0$ for $k = 1, \ldots, N_{\mathrm{h}}$, with the ILC time horizon N_{h}. The overall control law for the position controller is then given by $\tau_x^{\mathrm{d},j} = \tau_x^{\mathrm{c}} + \tau_x^{\mathrm{ilc},j}$. The overall control structure is depicted in Fig. 5.

As mentioned, the ILC design does not account for an additional load mass m_{L}. A direct consideration of m_{L} in the ILC design described previously would lead to recalculating the learning filter for different load masses. However, it is sufficient to scale the learning filter by $(m_{\mathrm{s}} + m_{\mathrm{L}})/m_{\mathrm{s}}$ to approximately account for an additional load mass m_{L} in the ILC.

The following implementation aspects turned out to be relevant for the ILC:

1) Experimental validations showed that reducing the damping factor α_k around the segment transitions is beneficial, especially for low velocities. This improves the convergence behavior of the learning. Therefore, the damping factor α_k is chosen depending on the shuttle position and, thus, on the sample point k. In the experiments, a damping factor of $\alpha_k = 0.75$ is used, which is gradually decreased to $\alpha_k = 0.5$ at the segment transitions for low velocities. These values were determined heuristically based on experiments on the test bench.
2) Due to the noncausality of the learning filter, the applied learned force $\tau_x^{\mathrm{ilc},j}$ is nonzero before the movement of the shuttle begins, i.e., before $\ddot{x}_s^{\mathrm{d}} \neq 0$.
3) It is meaningful to keep the learned additional force of the last sampling point within the ILC horizon $k = N_{\mathrm{h}}$ applied after the end of the trajectory. Otherwise, the shuttle would execute an unwanted movement if the additional force is set to zero at this point since the feedback controller cannot immediately compensate for this step-like disturbance.

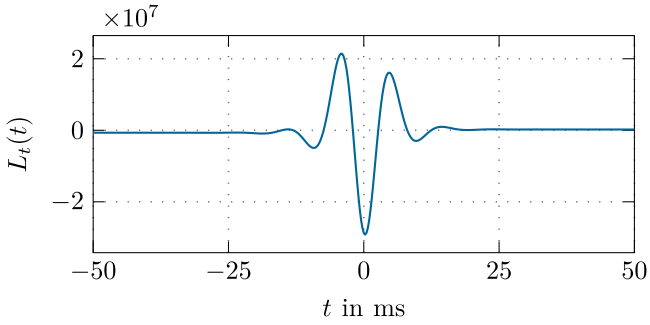

Fig. 4. Impulse response of the learning filter.

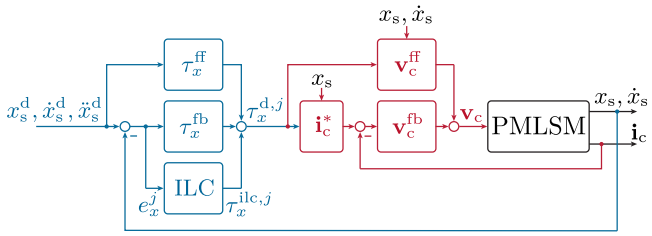

Fig. 5. Overall control structure with the force control loop in red and the position control loop in blue.

Two approaches for using the ILC in the position control loop are proposed in this work: 1) In the first approach, it is assumed that no specific information on the trajectory of the shuttle is known. It is, however, known from the industrial partner that high position tracking accuracy is particularly vital when a shuttle moves with constant velocity. During this phase, processing steps are undertaken on objects transported by the shuttle. Therefore, the ILC is applied for different constant velocities. After the ILC is converged, the resulting additional learned force $\tau_x^{\mathrm{ilc},j_{\mathrm{f}}}$ (j_{f} denotes the final ILC iteration) is stored in an LUT for a shuttle position grid $x_{\mathrm{s},\zeta}^{\tau} = \bar{x}_{\mathrm{s}}^{\tau} + \zeta\Delta_x^{\tau}, \zeta = 0, \ldots, N_{\mathrm{x}}^{\tau}$, with the start position of the LUT $\bar{x}_{\mathrm{s}}^{\tau}$, the grid width Δ_x^{τ}, and the number of grid points N_{x}^{τ}. The ILC is applied for shuttle velocities $\dot{x}_{\mathrm{s}} = \{\pm 0.1, \pm 0.25, \pm 0.5, \pm 0.75, \pm 1, \pm 1.5, \pm 2\}$m/s. After learning the LUT, a linear interpolation of the LUT using the current position and velocity is utilized during the operation of the PMLSM. 2) The second approach assumes that the shuttles execute repetitive tasks and move along known trajectories. In this case, an additional force for this specific trajectory is learned to achieve a high-precision position tracking along an entire trajectory. The learned force $\tau_x^{\mathrm{ilc},j_{\mathrm{f}}}$ is stored in an LUT for the sampling points k of the ILC horizon $1, \ldots, N_{\mathrm{h}}$ after the ILC is converged.

For both approaches, the learning is conducted at the final PMLSM setup after assembly, thus considering manufacturing and assembly tolerances. Relearning is, of course, possible to account for wear or other changes over time.

IV. Experimental Validation

This section presents the experimental validation of the presented method on a test bench, see Fig. 1. The test bench comprises a straight (SS), a curve (CS), and a circular arc segment (CAS). The total number of coils for this setup is $n_{\mathrm{c}} = 90$. The

segment transition between the SS and CS is at $x_\mathrm{s}/\nu_\mathrm{s} = 44$, and the segment transition between the CS and CAS is at $x_\mathrm{s}/\nu_\mathrm{s} = 74$. The control strategy is implemented in a dSpace SCALEXIO real-time system [43]. The current controller runs at a sampling time of $T_{\mathrm{s},i} = 25\ \mu$s, corresponding to the PWM switching frequency of 40 kHz for the half bridges. The PWM for each coil is generated on an FPGA with a time resolution of 8 ns. A trigger is utilized in the middle of the PWM to synchronize the processing unit with the FPGA, thus realizing a mid-center PWM. For the position control loop, a sampling time of $T_{\mathrm{s},x} = 250\ \mu$s is used. The controller parameters are chosen such that the bandwidth of the current and position controller is approximately 11 000 rad/s and 320 rad/s, respectively. Consequently, the subordinate current control loop dynamics can be neglected in the position controller design without compromising performance. The shuttle's position is measured with internal anisotropic magnetoresistive sensors, which allow the measurement of the shuttle's position with an accuracy of $\approx 5\ \mu$m, c.f., [37].

A. Optimal Force Control

In this section, the optimal force control strategy presented in Sections III-A and III-B is validated. A measurement shuttle holding a three-axis force/torque sensor is rigidly coupled with another position-controlled shuttle to assess the force control accuracy. A slow speed of 5 mm/s is used to obtain quasistationary measurements. The optimal current patterns from Section III-A are applied to the shuttle with the force/torque sensor. It is important to note that the force/torque sensor is only used for validation purposes and not in the control strategy. The desired and measured tractive forces τ_x^d and τ_x^m, and the force error $\tau_x^\mathrm{d} - \tau_x^\mathrm{m}$ for the CAS and CS are depicted in Fig. 6. These results show an excellent agreement between the measured and desired force. The error slightly increases at the ends of the CS, which might be related to a larger model-plant mismatch in the MEC model in this region. The slight offset error in the left part of the CS at higher forces is also related to a slightly larger model-plant mismatch. However, the overall force error is still very small and represents a significant improvement compared to standard FOC; see the comparison in [16]. Similar results are obtained for negative force values. These results are omitted for the sake of the brevity of this article.

B. Learning the LUT

This section presents the results for learning the LUT for different constant velocities (approach 1). The trajectory for learning is designed with a constant desired acceleration and deceleration $\ddot{x}_\mathrm{s}^\mathrm{d}$ with a maximum value of $\ddot{x}_{\mathrm{s,max}}^\mathrm{d} = 50\ \mathrm{m/s^2}$ to reach the desired maximum velocity $\dot{x}_{\mathrm{s,max}}^\mathrm{d}$ as fast as possible. The desired velocity and position trajectories are calculated by integrating the acceleration trajectory. A second-order low-pass filter is applied to the position, velocity, and acceleration to obtain sufficiently smooth trajectories. The desired trajectory used for learning for $\dot{x}_{\mathrm{s,max}}^\mathrm{d} = 0.25$ m/s is depicted in Fig. 7. For all other velocities, the same kind of trajectory is used.

Fig. 7 also depicts the measured position and velocity for the iteration $j = 0$ (i.e., the control strategy without ILC) and the final iteration $j = j_\mathrm{f}$ of the ILC. It is visible that large velocity errors occur at the segment transitions (around 2.45 s and 4.25 s for the positive velocity and 6 s and 7.8 s for the negative velocity) without ILC. This is because no highly accurate model is available for the segment transitions. The results for $j = j_\mathrm{f}$ show that the ILC can learn an additional force τ_x^ilc to significantly reduce the error.

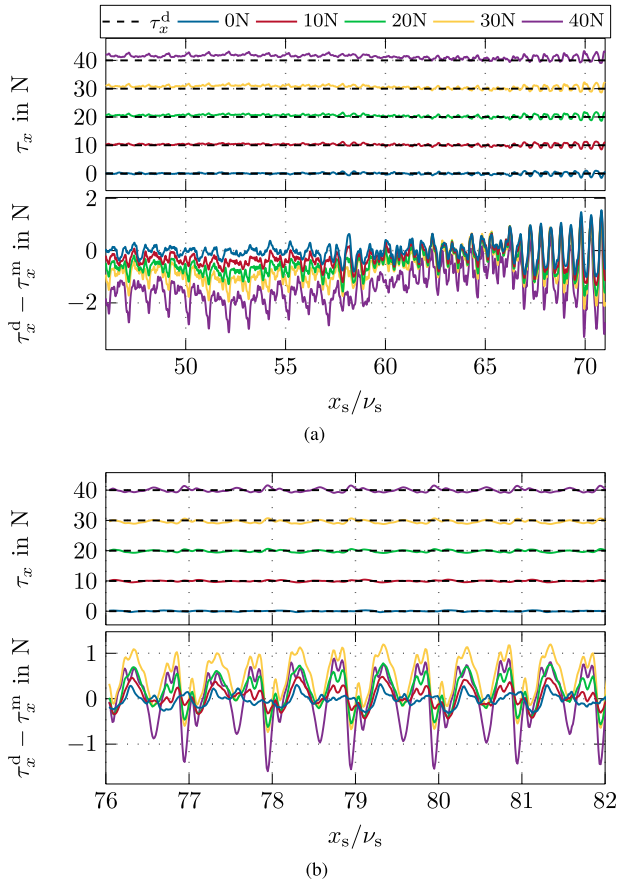

Fig. 6. Desired forces τ_x^d, measured forces τ_x^m, and the force error $\tau_x^\mathrm{d} - \tau_x^\mathrm{m}$ for (a) the CS and (b) the CAS.

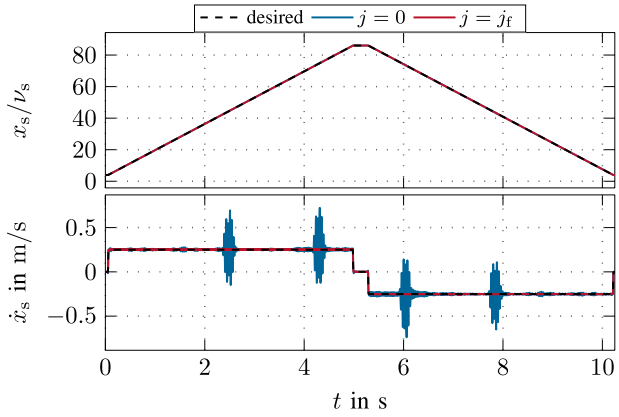

Fig. 7. Desired trajectory for learning the LUT for $\dot{x}_{\mathrm{s,max}}^\mathrm{d} = 0.25$ m/s, together with the position and velocity measurements of the zeroth and final iteration j_f of the ILC.

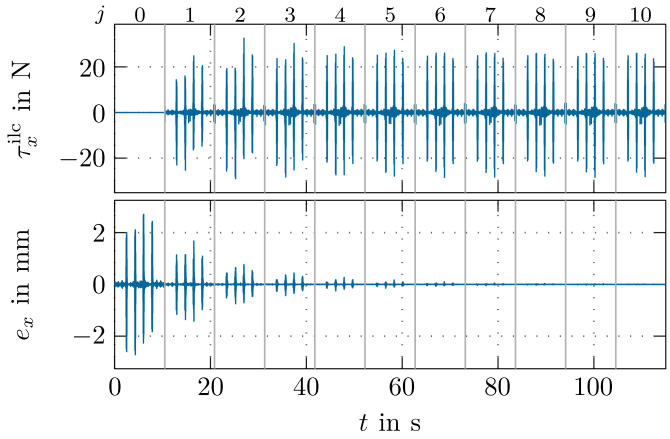

Fig. 8. Learned force τ_x^{ilc} and position error e_x for the first ten iterations for $\dot{x}_{\mathrm{s,max}}^{\mathrm{d}} = 0.25$ m/s.

Fig. 8 depicts the learned force τ_x^{ilc} and the position error e_x for the first ten iterations of the ILC. The position error e_x is already very small after the tenth iteration. In order to make sure that the ILC has converged to its optimum, 20 iterations are used for all velocities.

Fig. 9 shows a zoom of the positive velocity phase comparing the zeroth and final iteration to highlight the regions inside the segments for $\dot{x}_{\mathrm{s,max}}^{\mathrm{d}} = 0.25$ m/s. This zoom shows that the position tracking error inside the segments can also be significantly reduced by employing the presented ILC strategy compared to only using the optimum current patterns.

The results presented so far demonstrate that the ILC can increase position-tracking accuracy when combined with the optimal force control strategy. It is meaningful to study if a similar tracking accuracy can be achieved if the ILC is combined with a (less accurate) classical FOC strategy using sinusoidal current patterns. In the FOC, the desired force τ_x^{d} is proportional to the quadrature current $i_{\mathrm{q}}^{\mathrm{d}}$, and the direct current is set to zero $i_{\mathrm{d}}^{\mathrm{d}} = 0$ (no field weakening). The symmetric three-phase currents are calculated via the inverse dq0-transformation [44] and assigned to the respective coils. These currents are used in (5b). The results are shown in Fig. 9. In the zeroth iteration, where no additional force from the ILC is applied, the position tracking error is significantly larger than for the optimal currents. However, the presented ILC strategy is able to learn an additional force to achieve the same position-tracking accuracy for the FOC as for the optimal current control strategy. Thus, when used in combination with an ILC, the optimal current patterns do not bring an additional improvement in tracking accuracy compared to classical FOC.

However, another important aspect in the operation of a PMLSM is the efficiency, i.e., the ohmic losses P_{loss}. Fig. 10 proves that the averaged losses can be significantly reduced by employing the optimal current patterns for all desired velocities. A reduction of approximately 40% can be achieved, which is relevant since these reduced losses also imply lower temperatures of the coils during the operation of the PMLSM.

Based on these findings, two key advantages of employing optimal currents over the FOC can be identified. First, the tracking

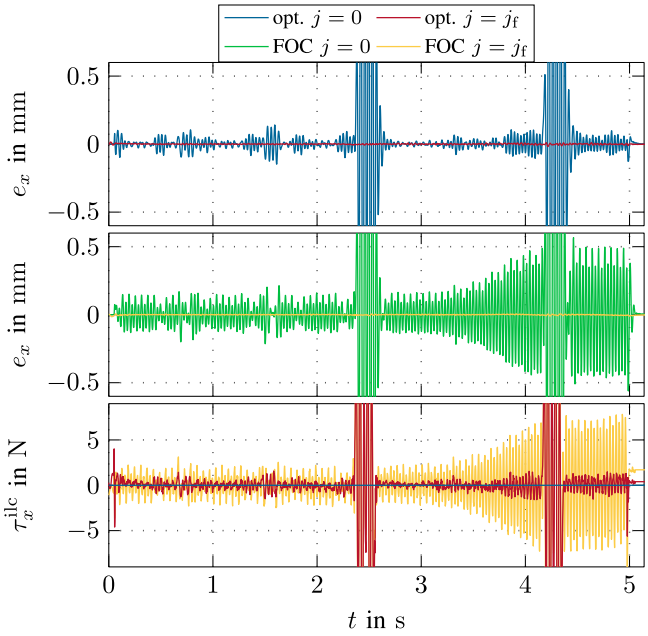

Fig. 9. Zoom of the learned force τ_x^{ilc} and position error e_x for the zeroth and final iteration for $\dot{x}_{\mathrm{s,max}}^{\mathrm{d}} = 0.25$ m/s comparing the strategy with optimal currents and the FOC approach.

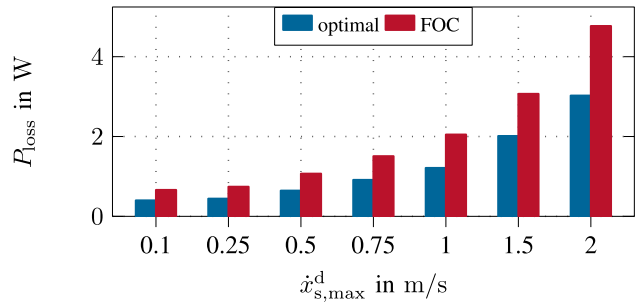

Fig. 10. Average ohmic losses for the final iteration at different desired velocities comparing the optimal current control strategy with the FOC approach.

accuracy is significantly better, especially for small velocities, without additional force from the ILC. This can be advantageous for regions of the motor where a good tracking performance without extremely high requirements should be achieved, and no extra effort must be made to learn an optimal compensation with the ILC. Second, the ohmic losses and, therefore, the heating-up of the coils are significantly reduced.

The position tracking error e_x for all velocities considered for obtaining the LUT are depicted in Fig. 11. For all velocities, the position tracking error is smaller than 20 μm and, in most cases, even smaller than 10 μm inside the segments, which is already in the range of the measurement accuracy of the position sensor. For high velocities (larger than 1 m/s), the error at the segment transitions (around $x_{\mathrm{s}}/\nu_s = 44$ and $x_{\mathrm{s}}/\nu_s = 74$) is slightly larger. This slightly increased error at high speed is of minor relevance for the practical application since very high accuracy is primarily relevant for low to medium-speed operations. While it would, in theory, be possible to increase

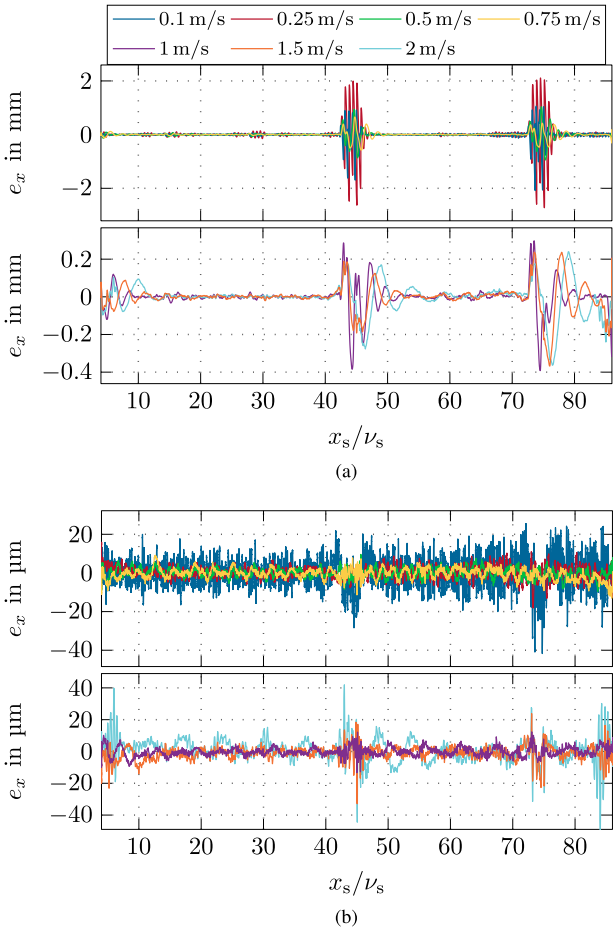

Fig. 11. Comparison of (a) the position error e_x without ILC and (b) the position error e_x after the final ILC iteration for different desired velocities $\dot{x}^{\mathrm{d}}_{\mathrm{s,max}}$.

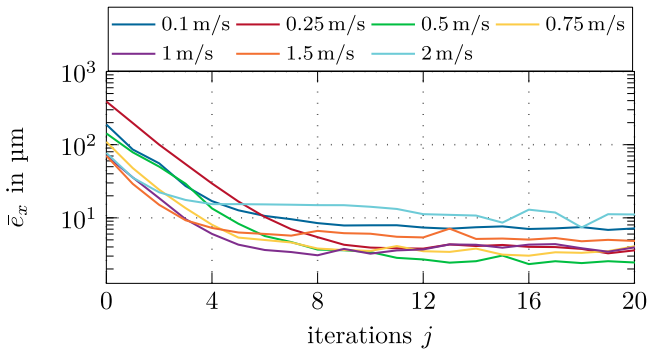

Fig. 12. RMS error $\bar{e}_x$ over the ILC iterations j for different desired velocities $\dot{x}^{\mathrm{d}}_{\mathrm{s,max}}$.

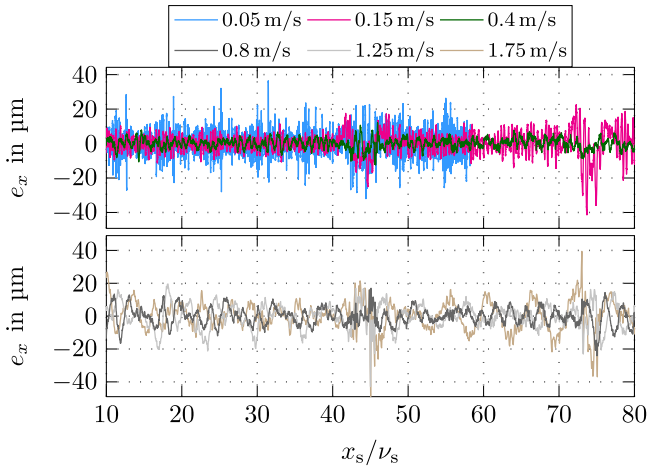

Fig. 13. Position error e_x for different desired velocities $\dot{x}^{\mathrm{d}}_{\mathrm{s,max}}$ that are not part of the LUT.

the tracking accuracy for high velocities (and thus these high-frequency errors), this would imply that large values for the coil voltages are required, resulting in reaching the control input limits, which is, of course, undesired. The residual error inside originates mainly from sensor noise and disturbances introduced by the rollers. Since this error is nonrepeating and stochastic, it cannot be reduced further. The results for negative velocities are omitted for conciseness but show equivalent results.

Remark 1: The typical operation range of the motor spans from low velocities (down to 0.05 m/s) to up to 2 m/s. In the high-velocity range, while smooth motion should be maintained, the position accuracy requirements are not as high. For low-velocity operations, both smooth motion and higher position accuracy are required, as products may be manipulated while moving along the stator on the shuttle.

Finally, in Fig. 12, the root-mean-square (RMS) error $\bar{e}_x = \sqrt{1/N_{\mathrm{h}} \sum_{\ell=1}^{N_{\mathrm{h}}} e_{x,\ell}^2}$ is plotted over the ILC iterations j for all learned velocities. This plot shows that a good convergence behavior of the ILC is obtained and that the choice of 20 iterations guarantees a solution close to the optimum.

As described before, the forces obtained by the ILC for the desired velocity are stored in an LUT on a position grid $x^{\tau}_{\mathrm{s},\zeta}$ (see Section III-D), resulting in a 2-D LUT. This LUT will be used in the next section to test if the proposed method yields an improved position accuracy in cases when the velocity differs from the values utilized in the generation of the LUT. Furthermore, it will be investigated if the additional forces learned for a specific shuttle are also suitable for a different shuttle, which might have small differences due to manufacturing tolerances.

C. Different Constant Velocities

Fig. 13 shows the position error for constant velocities that are not part of the LUT. It can be seen that also for these velocities, the position error is smaller than 20 μm over the larger parts of the motor length and even in the range of 10 μm for velocities smaller than 1.25 m/s. The errors are slightly larger only at the segment transitions. This result agrees with results obtained for the velocities used for learning the LUT and, thus, proves that high-precision position tracking is attained for constant velocities in the entire motor operation range.

D. Application of the LUT to Other Shuttles

For the following experiments, the LUT is learned for shuttle 1 (see Section IV-B) and applied to three other shuttles (shuttle 2 to shuttle 4). The resulting position error e_x is shown in Fig. 14. It

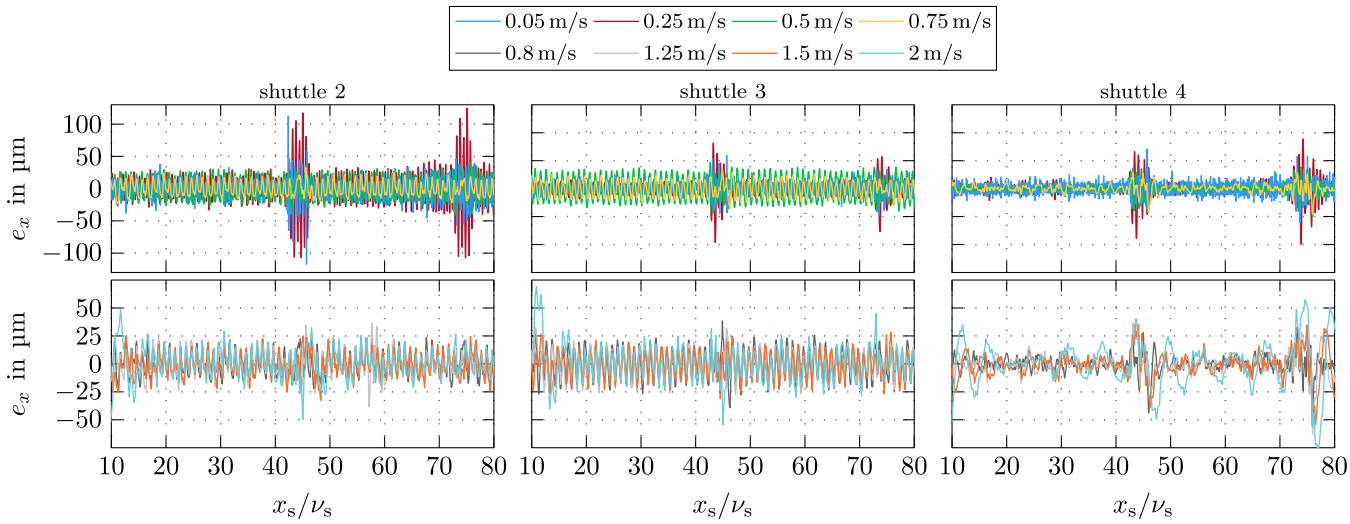

Fig. 14. Position error e_x for different desired velocities $\dot{x}^{\mathrm{d}}_{\mathrm{s,max}}$ and three different shuttles (shuttle 2 to shuttle 4).

can be seen that the LUT learned for one shuttle translates well to other shuttles, showing the presented method's robustness concerning manufacturing tolerances. The errors are slightly larger than for shuttle 1 due to tolerances in the mounting, magnetization of the permanent magnets, and manufacturing tolerances in the shuttles. However, high-precision tracking is achieved for all shuttles with an error smaller than 40 μm for all shuttles and velocities inside the segments. For higher velocities (from 0.75 m/s to 1.75 m/s), an error as low as 25 μm can be achieved. Only for shuttle 2 at a velocity of 0.25 m/s the error rises to 100 μm, which is, however, still a significant improvement compared to the tracking error without ILC. This increased error is because shuttle 2 shows the largest deviations among all shuttles compared to shuttle 1. These deviations originate from variations in the magnetization of the PMs and the mounting and manufacturing tolerances of the shuttle, including the PMs' placement. Of course, separate learning for each shuttle would be possible with the presented method, resulting in even smaller position errors (see Section IV-B). However, this might not be very efficient if many shuttles are utilized in the PMLSM.

E. Different Trajectories

Up to now, the position accuracy has been evaluated primarily for constant shuttle velocities. This section evaluates the achievable position accuracy for a more complex trajectory. Moreover, the two approaches described in Section III-D are compared, i.e., approach 1, where the LUT is learned for constant velocities, and approach 2, where the LUT is learned for the specific trajectory. The trajectory (traj1) used consists of multiple acceleration, deceleration, and constant velocity phases, and the velocity is chosen to reach a maximum of $\dot{x}^{\mathrm{d}}_{\mathrm{s,max}} = 2$ m/s. The experiments in this section are conducted with shuttle 1.

Fig. 15 shows the results for traj1 for the case without ILC (no ILC), the LUT learned in Section IV-B (LUT), and the ILC learned for the specific trajectory (ILC). Good trajectory tracking is already possible without ILC, but a significant improvement is achieved when applying the learned LUT. The ILC learned

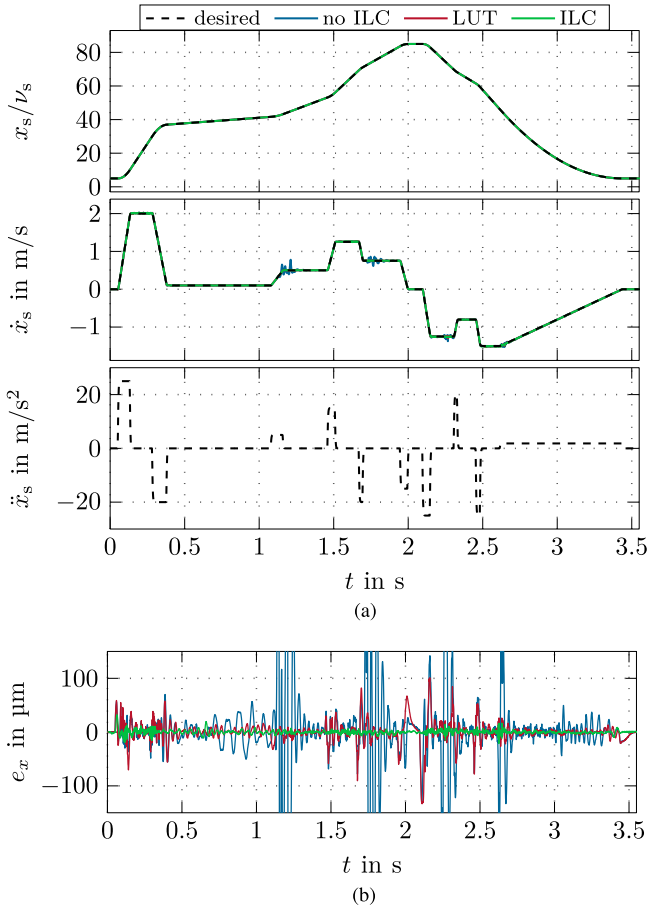

Fig. 15. Tracking results for traj1 without ILC (no ILC), with the use of the learned LUT, and with learning conducted specifically for traj1 (ILC): (a) desired trajectory, measured position and velocity, and (b) position error.

for the specific trajectory further increases the position accuracy, particularly during the acceleration and deceleration phases.

When using the optimal currents, the ohmic losses are reduced from 1.62 W for the FOC to 0.97 W. This shows that increased efficiency is also obtained for more complex trajectories.

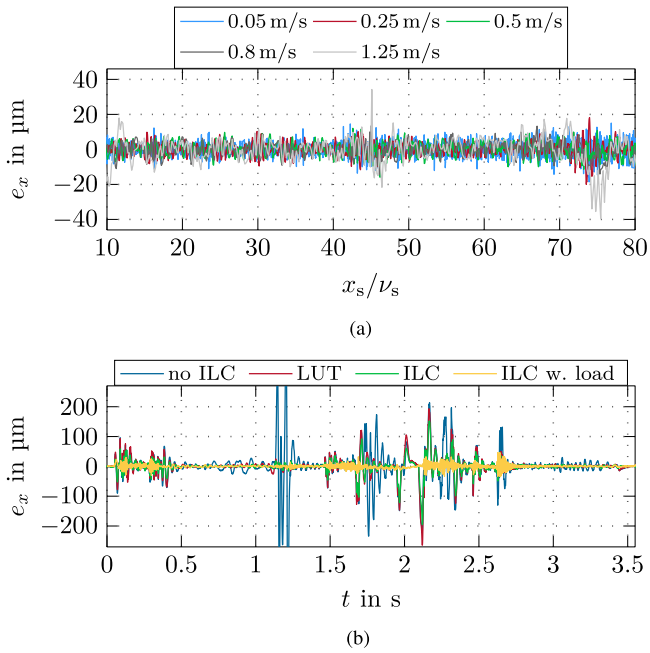

Fig. 16. Position error for the validation scenarios with an additional mass load of 0.66 kg (a) for different desired constant velocities $\dot{x}^{\mathrm{d}}_{\mathrm{s,max}}$ and (b) for traj1.

F. Additional Shuttle Load

The final experiment is related to the influence of the approximately known additional load mass on the shuttle. For this, an additional load mass of $m_{\mathrm{L}} = 0.66$ kg is mounted on the shuttle, where the empty shuttle has a mass of $m_{\mathrm{s}} = 0.73$ kg, i.e., the overall mass is increased by 90%. The approximately known additional load mass m_{L} was considered in the position controller (6) for the following experiments.

The results for the validations with an additional load are depicted in Fig. 16. Fig. 16(a) shows the position error for constant velocities using the LUT learned in Section IV-B without load mass. It can be seen that the same high-precision position tracking performance is achieved as for the case without additional load [see Fig. 11(b) and Fig. 13]. The position tracking error is as low as 10 μm. Only for higher velocities, i.e., 1.25 m/s, does the error slightly increase during the segment transitions. No higher velocities are used with the load to avoid violating the control input limit. As expected, the additional load mass does not influence the position accuracy in the constant speed operation, see Fig. 16(a).

For the experiments with traj1, four cases are compared: optimal force controller without additional force (no ILC), with the LUT from Section IV-B (LUT), with the ILC learned on the shuttle without additional load and applied to the shuttle with load (ILC), and the ILC learned and applied to the shuttle with load (ILC w. load). The results depicted in Fig. 16(b) show that the position tracking error is again vastly reduced with the presented method. As expected, applying ILC results obtained without load mass to cases with additional load mass leads to larger errors, particularly during the acceleration and deceleration phases. However, using ILC learning specifically adapted for the case with load mass significantly improves accuracy, achieving levels similar to those without load mass. Thus, it makes sense to perform the learning of the ILC for a specific trajectory for the final system, including the load mass. Nonetheless, if this is not possible, a significant improvement can still be obtained compared to the FOC or the optimal control without ILC.

V. Conclusion

This work presents a high-precision position tracking control strategy for segmented stator PMLSMs. The strategy calculates optimal currents for the curved segments to track a desired tractive force and minimize the sum current and the ohmic losses. This results in a remarkable 40% increase in motor energy efficiency. A superimposed two-degree-of-freedom position controller is extended with a stochastically optimal ILC, enabling high-precision position tracking over the entire curvilinear track of the considered PMLSM. Validations on a test bench demonstrate the effectiveness and robustness of this method. By acquiring an LUT for constant velocities using the presented ILC strategy, high-precision position tracking can be achieved for most industrially relevant use cases. The strategy also applies to arbitrary repeating trajectories, further improving tracking accuracy. Importantly, the method does not require additional telemetry and comes with low computational costs, making it readily applicable to final PMLSM setups with minimal effort. Future research will focus on the coordinated control of multiple shuttles to achieve high-precision position tracking in close proximity operations and examine cooperative force control between shuttles.

Acknowledgment

The authors acknowledge TU Wien Bibliothek for financial support through its Open Access Funding Programme.

References

[1] M. Mihalachi, R. Leidhold, and P. Mutschler, "Motion control for long primary linear drives used in material handling," in *Proc. 14th Int. Power Electron. Motion Control Conf.*, Ohrid, Macedonia, 2010, pp. T5-94–T5-101.

[2] T. Zhang, X. Mei, and X. Du, "A new winding segmented permanent magnet linear synchronous motor for multiple passive carriers," *IEEE Trans. Magn.*, vol. 58, no. 7, pp. 1–9, Jul. 2022.

[3] C. Krämer, A. Kugi, and W. Kemmetmüller, "Optimal force control of a permanent magnet linear synchronous motor with multiple shuttles," *ISA Trans.*, vol. 140, pp. 483–489, 2023.

[4] S. Makino et al., "Consideration of linear synchronous motor characteristic in curved part," in *Proc. 11th Int. Symp. Linear Drives Ind. Appl.*, Osaka, Japan, 2017, pp. 1–6.

[5] Y. Liu, X. Huang, and W. Yu, "Topology analysis and thrust optimization of arc permanent magnet linear synchronous motor," in *Proc. 13th Int. Symp. Linear Drives Ind. Appl.*, Wuhan, China, 2021, pp. 1–5.

[6] Y. Liu, X. Huang, J. Li, and W. Yu, "Magnetic field analysis and thrust optimization of arc permanent magnet synchronous motor combined with linear mover and arc stator," *IEEE Trans. Ind. Appl.*, vol. 59, no. 5, pp. 5867–5874, Sep.–Oct. 2023.

[7] J. F. Gieras, *Linear Synchronous Motors: Transportation and Automation System*. Boca Raton, FL, USA: CRC Press, 2000.

[8] M. A. M. Cheema and J. E. Fletcher, *Advanced Direct Thrust Force Control of Linear Permanent Magnet Synchronous Motor*. Cham, Switzerland: Springer, 2020.

[9] J. Chiasson, D. Seto, F. Sun, A. Stankovic, and S. Bortoff, "Control of two PM linear motors with a single inverter: Application to elevator doors," *Mechatronics*, vol. 15, no. 1, pp. 95–110, 2005.
[10] R. Cao, M. Cheng, and B. Zhang, "Speed control of complementary and modular linear flux-switching permanent-magnet motor," *IEEE Trans. Ind. Electron.*, vol. 62, no. 7, pp. 4056–4064, Jul. 2015.
[11] A. Wang, L. Li, and X. Huang, "Modified robust predictive current control design of windings-discontinuous-segmented PMLSM based on an improved analysis method," *IEEE Trans. Power Electron.*, vol. 40, no. 1, pp. 774–786, Jan. 2025.
[12] Y.-S. Huang and C.-C. Sung, "Function-based controller for linear motor control systems," *IEEE Trans. Ind. Electron.*, vol. 57, no. 3, pp. 1096–1105, Mar. 2010.
[13] Y. Zhang, J. Zhu, W. Xu, and Y. Guo, "A simple method to reduce torque ripple in direct torque-controlled permanent-magnet synchronous motor by using vectors with variable amplitude and angle," *IEEE Trans. Ind. Electron.*, vol. 58, no. 7, pp. 2848–2859, Jul. 2011.
[14] M. A. M. Cheema, J. E. Fletcher, M. F. Rahman, and D. Xiao, "Optimal, combined speed, and direct thrust control of linear permanent magnet synchronous motors," *IEEE Trans. Energy Convers.*, vol. 31, no. 3, pp. 947–958, Sep. 2016.
[15] M. Abroshan, J. Milimonfared, K. Malekian, and A. Rahnamaee, "An optimal control for saturated interior permanent magnet linear synchronous motors incorporating field weakening," in *Proc. 13th Int. Power Electron. Motion Control Conf.*, Poznan, Poland, 2008, pp. 1117–1122.
[16] C. Krämer, A. Kugi, and W. Kemmetmüller, "Optimal force control of a permanent magnet linear synchronous motor based on a magnetic equivalent circuit model," *Control Eng. Pract.*, vol. 122, 2022, Art. no. 105076.
[17] R. Hosseinzadeh, F. Martin, and M. Hinkkanen, "Energy-efficient control of bearingless linear motors," in *Proc. IEEE Int. Conf. Mechatron.*, Loughborough, U.K., 2023, pp. 1–6.
[18] H. H. Mu, Y. F. Zhou, X. Wen, and Y. H. Zhou, "Calibration and compensation of cogging effect in a permanent magnet linear motor," *Mechatronics*, vol. 19, no. 4, pp. 577–585, 2009.
[19] C. Röhrig and A. Jochheim, "Identification and compensation of force ripple in linear permanent magnet motors," in *Amer. Control Conf.*, vol. 3, Arlington, TX, USA, 2001, pp. 2161–2166.
[20] L. Bascetta, P. Rocco, and G. Magnani, "Force ripple compensation in linear motors based on closed-loop position-dependent identification," *IEEE/ASME Trans. Mechatron.*, vol. 15, no. 3, pp. 349–359, Jun. 2010.
[21] H.-S. Ahn, Y. Chen, and H. Dou, "State-periodic adaptive compensation of cogging and coulomb friction in permanent-magnet linear motors," *IEEE Trans. Magn.*, vol. 41, no. 1, pp. 90–98, Jan. 2005.
[22] K. K. Tan, T. H. Lee, H. F. Dou, S. J. Chin, and S. Zhao, "Precision motion control with disturbance observer for pulsewidth-modulated-driven permanent-magnet linear motors," *IEEE Trans. Magn.*, vol. 39, no. 3, pp. 1813–1818, May 2003.
[23] M. Wang, L. Li, and D. Pan, "Detent force compensation for PMLSM systems based on structural design and control method combination," *IEEE Trans. Ind. Electron.*, vol. 62, no. 11, pp. 6845–6854, Nov. 2015.
[24] F. Song, Y. Liu, J. X. Xu, X. Yang, P. He, and Z. Yang, "Iterative learning identification and compensation of space-periodic disturbance in PMLSM systems with time delay," *IEEE Trans. Ind. Electron.*, vol. 65, no. 9, pp. 7579–7589, Sep. 2018.
[25] M. Wang, K. Kang, C. Zhang, and L. Li, "Precise position control in air-bearing PMLSM system using an improved anticipatory fractional-order iterative learning control," *IEEE Trans. Ind. Electron.*, vol. 71, no. 6, pp. 6073–6083, Jun. 2024.
[26] X. Zhang, L. Xiao, S. Li, J. Zou, Y. Xu, and G. Yu, "Velocity ripple suppression of APMSM via iterative learning sliding mode control considering coil switching," *IEEE J. Emerg. Sel. Topics Power Electron.*, vol. 13, no. 1, pp. 652–663, Feb. 2025.
[27] K. Cho and K. Nam, "Robust periodic adaptive disturbance observer based control considering long-term instability problems for high-load motion systems," *IEEE Trans. Ind. Electron.*, vol. 69, no. 6, pp. 6258–6266, Jun. 2022.
[28] Z. Liu, X. Yu, W. Lin, and J. J. Rodríguez-Andina, "Iterative learning observer-based high-precision motion control for repetitive motion tasks of linear motor driven systems," *IEEE Open J. Ind. Electron. Soc.*, vol. 5, pp. 54–66, 2024.
[29] G. Zhang et al., "PR internal mode extended state observer-based iterative learning control for thrust ripple suppression of PMLSM drives," *IEEE Trans. Power Electron.*, vol. 39, no. 8, pp. 10095–10105, Aug. 2024.
[30] Q. Huang, X. Huang, W. Yu, and C. Ren, "Modeling and optimization of detent force for flexible permanent magnet synchronous linear motor considering spacing between primaries," in *Proc. 13th Int. Symp. Linear Drives Ind. Appl.*, Wuhan, China, 2021, pp. 1–6.
[31] J. H. Kim, S. W. Jung, Y. S. Kwon, S. Lee, and J. Y. Yoon, "Modeling of current-driven end-effect force ripple in air-cored linear synchronous motor with multiple modular stators," *IEEE Trans. Ind. Electron.*, vol. 70, no. 11, pp. 11507–11515, Nov. 2023.
[32] J. M. M. Rovers, J. W. Jansen, and E. A. Lomonova, "Novel force ripple reduction method for a moving-magnet linear synchronous motor with a segmented stator," in *Int. Conf. Elect. Machines Syst.*, Wuhan, China, 2008, pp. 2942–2947.
[33] N. Nevaranta, M. Huikuri, M. Niemelä, and J. Pyrhönen, "Cogging force compensation of a discontinuous permanent magnet track linear motor drive," in *Proc. 19th Eur. Conf. Power Electron. Appl.*, Warsaw, Poland, 2017, pp. P.1–P.7.
[34] G. Fuchs, A. Kugi, and W. Kemmetmüller, "Magnetic equivalent circuit modeling of a permanent magnet linear synchronous motor composed of curved segments," *Mechatronics*, vol. 104, 2024, Art. no. 103256.
[35] C. Krämer, A. Kugi, and W. Kemmetmüller, "Modeling of a permanent magnet linear synchronous motor using magnetic equivalent circuits," *Mechatronics*, vol. 76, 2021, Art. no. 102558.
[36] *ACOPOStrak Users Manual*. Eggelsberg, Austria: B&R Ind. Autom. GmbH, 2024.
[37] G. Fuchs, A. Deutschmann-Olek, A. Kugi, and W. Kemmetmüller, "Iterative learning-based online calibration of a position sensor system for permanent magnet linear synchronous motors," in *Proc. 50th Annu. Conf. IEEE Ind. Electron. Soc.*, Chicago, IL, USA, 2024, pp. 1–8.
[38] L. N. Trefethen, *Spectral Methods in MATLAB*. Philadelphia, PA, USA: SIAM, 2000.
[39] J. P. Boyd, *Chebyshev and Fourier Spectral Methods*. Mineola, NY, USA: Dover, 2000.
[40] V. Ostović, *Dynamics of Saturated Electric Machines*. New York, NY, USA: Springer, 1989.
[41] H. K. Khalil, *Nonlinear Systems*, 3rd Ed. Upper Saddle River, NJ, USA: Prentice-Hall, 2002.
[42] A. Deutschmann-Olek, G. Stadler, and A. Kugi, "Stochastic iterative learning control for lumped- and distributed-parameter systems: A wiener-filtering approach," *IEEE Trans. Autom. Control*, vol. 66, no. 8, pp. 3856–3862, Aug. 2021.
[43] dSPACE, *SCALEXIO Product Information*. Paderborn, Germany: dSPACE, 2022.
[44] I. Boldea and S. A. Nasar, *Linear Electric Actuators and Generators*. Cambridge, U.K.: Cambridge Univ. Press, 2009.

Gerd Fuchs (Graduate Student Member, IEEE) received the Dipl.-Ing. degree in energy systems and automation technology from TU Wien, Vienna, Austria, in 2021.

He is currently a Research Assistant with the Automation and Control Institute, TU Wien. His research interests include the physics-based modeling and control of electric machines with a special focus on permanent magnet linear synchronous motors.

Andreas Deutschmann-Olek (Member, IEEE) received the Dipl.-Ing. and Ph.D. degrees in control engineering from TU Wien, Vienna, Austria, in 2014 and 2019, respectively.

He is currently an Assistant Professor with the Automation and Control Institute, TU Wien. His main research interest comprises control, estimation, and learning methods for nonlinear and infinite-dimensional systems with a strong focus on applications to photonic and quantum systems.

Andreas Kugi (Senior Member, IEEE) received the Dipl.-Ing. degree in electrical engineering from TU Graz, Graz, Austria, in 1992. He earned his Ph.D. in Control Engineering in 1995 and his habilitation in Automatic Control and Control Theory in 2000, both from Johannes Kepler University Linz (JKU), Austria.

From 2000 to 2002 he served as Associate Professor at JKU, and from 2002 to 2007 he was Full Professor at Saarland University, Saarbrücken, Germany. Since 2007 he has held the Chair of Complex Dynamical Systems at the Automation and Control Institute (ACIN), TU Wien, Vienna, Austria. Since July 2023, he has been Scientific Director of the AIT Austrian Institute of Technology, Vienna, after having directed its Center for Vision, Automation and Control from 2017 to 2023. His research focuses on modelling, control, and optimization of complex dynamical systems, mechatronic system design, robotics, and process automation.

Prof. Kugi is a Full Member of the Austrian Academy of Sciences and a Member of the German National Academy of Science and Engineering (acatech).

Wolfgang Kemmetmüller (Member, IEEE) received the Dipl.-Ing. degree in mechatronics from Johannes Kepler University, Linz, Austria, in 2002, the Ph.D. (Dr. Ing.) degree in control engineering from Saarland University, Saarbrücken, Germany, in 2007, and the habilitation degree in system theory and automatic control from TU Wien, Vienna, Austria, in 2017.

He is currently a Full Professor with the Automation and Control Institute, TU Wien. His research interests include physics-based modeling and nonlinear control of mechatronic systems with a special focus on power electronics, electrical machines, and large-scale robotic systems.